Symmetry breaking of the persistent spin helix in quantum transport

Pirmin J. Weigele,[1] D. C. Marinescu,[2] Florian Dettwiler,[1] Jiyong Fu,[3] Shawn Mack,[4] J. Carlos Egues,[5]
David D. Awschalom,[6] and Dominik M. Zumbühl[1]
[1]*Department of Physics, University of Basel, CH-4056, Basel, Switzerland*
[2]*Department of Physics and Astronomy, Clemson University, Clemson, South Carolina 29634, USA*
[3]*Department of Physics, Qufu Normal University, Qufu, Shandong, 273165, China*
[4]*U.S. Naval Research Laboratory, Washington, DC 20375, USA*
[5]*Instituto de Física de São Carlos, Universidade de São Paulo, 13560-970 São Carlos, São Paulo, Brazil*
[6]*Institute for Molecular Engineering, University of Chicago, Chicago, Illinois 60637, USA*

(Received 27 October 2017; revised manuscript received 8 December 2019; published 16 January 2020)

We exploit the high-symmetry persistent spin helix state obtained for similar Rashba and linear Dresselhaus interactions in a quantum well to revisit the weak localization problem within a perturbative approach in a Landau level formulation. We define the small parameter of the theory as the deviation from the symmetry state introduced by the mismatch of the linear terms and by the strength of the cubic Dresselhaus term. In the vicinity of the helix state, the SO field becomes uniaxial, offering a natural direction of spin quantization, thus defining the z axis within the 2D plane. In contrast to previous theories, this reveals a full decoupling of the Cooperon triplet scattering modes as well as decoupled Landau levels, to lowest order in the small parameter. This makes it possible to derive a closed-form expression for the weak localization magnetoconductivity, thus providing a new paradigm of localization in the weakly-broken spin symmetry regime. We perform quantum transport experiments in GaAs quantum wells, finding very good agreement with the new theory. We present a reliable two-step method to extract the SO and transport parameters from fits of the new expression, obtaining excellent agreement with recent experiments. This is an important step towards engineering and controlling the spin-orbit interaction as a powerful resource in emerging quantum technologies.

DOI: 10.1103/PhysRevB.101.035414

I. INTRODUCTION

The spin-orbit (SO) interaction is of profound importance for a broad range of phenomena in modern condensed matter physics, such as spin textures [1,2], spin Hall effects [3,4], topological insulators [5–8], and Majorana fermions [9,10], as well as for application in spintronics [11,12] and quantum computation [13–15]. Semiconductors such as GaAs, InAs, or InSb offer various strengths of SO coupling combined with a high level of electrical control [16–23] over the SO parameters, e.g., in quantum wells and are thus suitable for a broad range of experiments. The two dominant contributions to SO coupling in semiconductor quantum wells arise from breaking of structural and bulk inversion symmetry, quantified by the Rashba coefficient α and the Dresselhaus coefficient γ, respectively. While the Rashba effect [24] is linear in electron momentum, the bulk Dresselhaus [25] term is cubic. When projected into a quantized 2D system as in a 2D electron gas (2DEG), it retains a cubic component with coefficient β_3 but also acquires a linear component of strength β.

A particularly interesting situation arises when $\alpha = \beta$: A persistent spin helix (PSH) can be formed [26,27], which is robust against D'yakonov Perel scattering, strongly suppressing spin relaxation [28]. In this state, spins do not precess at all when traveling ballistically along one particular direction in the 2D plane, while precessing quickly when proceeding along the orthogonal direction in the 2D plane. Effectively, spin symmetry is restored by a complete cancellation of the Rashba and linear Dresselhaus terms along one direction and the creation of a uniaxial internal SO field—a new unique in-plane spin quantization axis—broken only by the cubic Dresselhaus term and by a deviation from $\alpha = \beta$.

With optical methods, the SO parameters can be readily extracted from experiments [28–36] by monitoring a spin component directly, e.g., with Kerr rotation methods. This is much more difficult to achieve from electronic transport measurements where the spin information is not usually directly accessible. In materials with strong SO coupling, the beating patterns of the Shubnikov de-Haas oscillations can sometimes be used to extract the Rashba parameter [16–19,37]. Even if SO coupling is weak, quantum interference effects depend very sensitively on the spin of the electron, giving weak antilocalization (WAL) as the paradigmatic signature of SO coupling in quantum transport experiments. To extract the SO parameters from such highly-sensitive magnetoconductance measurements, one needs to rely on a model containing the relevant SO terms. For some special cases, it was possible to derive closed-form expressions already early-on: with cubic terms only [38,39], without SO terms altogether [38,40], or for precisely the spin helix point $\beta = \pm\alpha$ and $\beta_3 = 0$, in which case weak localization (WL) was recovered [41] as if there were no SO coupling at all.

Here, we investigate WL and WAL corrections to the conductivity both theoretically and experimentally in a GaAs 2DEG around the spin helix state. This regime—predicted [26,27] and realized recently [28] and in further experiments [21,42]—affords a new opportunity for calculating the magnetoconductance by offering a high symmetry point ($\alpha = \beta$) around which a new small parameter may be introduced: the deviation from the perfect spin symmetry, via imperfectly matched linear terms $\propto \alpha - \beta$ or through the cubic term $\propto \beta_3$. In both cases of broken spin symmetry, the effective SO field remains small, i.e., the WAL minima occur at small magnetic field, thus remaining in the spin diffusive regime. We note that $\alpha + \beta$ is assumed to be large compared to $\alpha - \beta$, i.e., both linear terms may individually be large, such that, e.g., pronounced antilocalization would result in the absence of the other term, even for $\beta_3 = 0$. This is substantially different from the case when Rashba and linear Dresselhaus are *both* equal to zero, i.e., without linear SO coupling. There appear also terms which are proportional to the sum $\alpha + \beta$, and these are large and retained here and give a shift of the polarized triplets in momentum space.

With the choice of the emergent axis of spin quantization in the spin helix regime as the new z axis, a decoupling of the Cooperon triplet scattering modes to lowest order in the new small parameter becomes apparent, shown in Fig. 1(a), as well as a decoupling of the Landau levels into which the scattering modes are expanded in the presence of a perpendicular magnetic field. Given these important simplifications around the symmetry point, it is now possible to derive a new closed-form expression including simultaneously both linear SO terms as well as the cubic term in the vicinity of the PSH point. This provides a new paradigm of localization for the weakly broken spin symmetry regime.

Next, we put the new theory to test against experiment in the same regime and find very good agreement. Further, we develop a reliable method to extract all relevant SO parameters from quantum transport data using the new expression. This method exploits the cancellation of the linear terms to extract, in a first step, independently the cubic term and phase coherence in the high carrier density regime where the cubic term already breaks spin symmetry and restores WAL. Then, in a second step, we tune slightly away from $\alpha = \beta$ and can now also extract the linear SO parameters, again from fits to the new theory. This two step procedure delivers all SO parameters and finds very good agreement with recent transport studies [23,43] as well as optical experiments [34,44,45]. In particular, we extract a Dresselhaus material parameter $\gamma = 11.5 \pm 1$ eV Å^3 in good agreement with recent experiments.

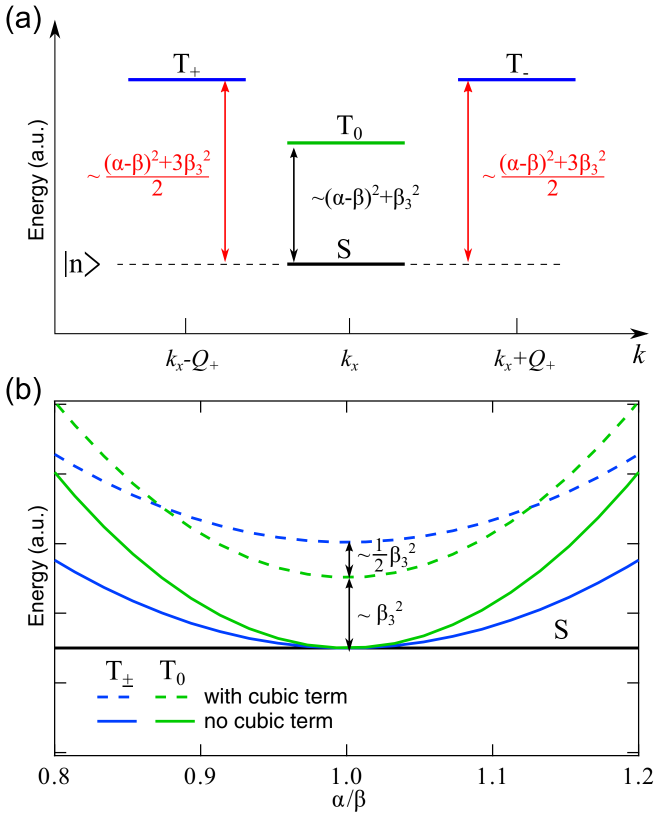

FIG. 1. Cooperon terms around the PSH symmetry $\alpha = \beta$, with singlet (S) and triplet (T_0, $T_\pm$) states all in the same, generic Landau level $|n\rangle$. (a) Energy of the Cooperon eigenstates as functions of k_x, the Cooperon momentum along $\hat{x}$ which fixes the center of the orbit. The S and T_0 states are located at k_x and become degenerate at $\alpha = \beta$ and $\beta_3 = 0$. T_+ and T_- are degenerate, but since the orbits are separated by $2Q_+$ there is no coupling between them, giving WL. Note there is no coupling to other Landau levels. (b) Energies of the eigenstates in one Landau level as a function of the ratio of α/β. The full curves correspond to the case where the cubic term is zero and all states are degenerate at $\alpha = \beta$ and WL is observed. The dashed lines correspond to the states, when the cubic term is strong, then S and T_0 state are not degenerate at $\alpha = \beta$ giving WAL even at $\alpha = \beta$.

II. QUANTUM CORRECTIONS TO CONDUCTIVITY

There is a large body of literature addressing the subject of quantum corrections over the past decades: Already the very early work of Hikami, Larkin, and Nagaoka [38] includes SO effects in the form of generic impurity scattering (skew scattering) in the diffusive regime and is the only work to date to provide a closed-form expression in the presence of SO interaction and a magnetic field. The effect of an in-plane magnetic field was also discussed soon after [46]. For the case of III-V semiconductors, the Dyakonov-Perel mechanism [47] is prevalent in the diffusive regime. Iordanskii *et al.* Ref. [48] consider the linear and cubic Dresselhaus terms in the absence of the Rashba term, but in the presence of a magnetic field in the Landau quantized formulation, providing an analytical but not closed-form expression. The standard Cooperon structure with coupled triplet modes and mixing between adjacent Landau levels was established [41,48,49]. Pikus and Pikus, Ref. [41], as well as Knap *et al.* [49] generalized this formalism to include also the Rashba term, together with the cubic Dresselhaus term, but not both Rashba and linear Dresselhaus terms at the same time. A similar expression as in Ref. [48] is obtained when only the Rashba term is retained [50]. The same formalism was also applied to include in-plane magnetic fields [51]. To date, a closed form in the fully Landau quantized formulation could not be found for the generic case with both Rashba and linear as well as cubic Dresselhaus terms *due to the coupled Cooperon and Landau level structure*, only numerical solutions were available [41,49].

Beyond the diffusive regime, only skew scattering was considered [52,53] and had to be solved numerically. Both Rashba and Dresselhaus terms could be treated but only numerically and without fully taking into account coherent interference effects between the terms [54]. More complete numerical models exist for either only Rashba or only linear Dresselhaus terms [55] or also for all three terms [56–58]. Antilocalization was also considered in quantum wires [59], and the PSH was studied for various crystal orientations [60] and in two-subband wells [61] in which crossed PSHs lead to topological skyrmionic spin textures in ordinary GaAs wells [62].

Only recently, a closed form expression valid for arbitrary values of all three SO coupling parameters was derived in a semiclassical formalism in momentum formulation [63]. In contrast, here we present a completely Landau quantized treatment of the localization problem that exploits the PSH high spin-symmetry point.

A. The PSH high symmetry point

Here, we consider a 2D electron gas in the $\hat{x}$-$\hat{z}$ plane with the $\hat{y}$ axis denoting perpendicular direction. This particular choice of coordinates takes into account the new in-plane spin quantization axis as the $\hat{z}$ direction at the symmetry point $\alpha = \beta$. The single particle Hamiltonian corresponding to an electron of effective mass m^*, momentum $\mathbf{p} = \{p_x, p_y, p_z\}$, and spin $\sigma = \{\sigma_x, \sigma_y, \sigma_z\}$ with Rashba and Dresselhaus SO coupling reads

$$H_{\mathbf{p}} = \frac{p_x^2 + p_z^2}{2m^*} + \alpha(\sigma_z p_x - \sigma_x p_z) + \beta_1(\sigma_z p_z - \sigma_x p_x) - \gamma\left(\sigma_z p_z p_x^2 - \sigma_x p_x p_z^2\right), \quad (1)$$

where β_1 is the bare linear Dresselhaus coefficient. This choice of coordinates highlights the existence of a $\hat{z}$ in-plane axis, obtained through a $\pi/4$ in-plane rotation to be parallel to $[1\bar{1}0]$ ($\hat{x} \parallel [110]$), that becomes the quantization axis for the electron spin. At $\alpha = \beta$ the spin projection on this axis is a good quantum number of the system, a property not immediately apparent if one chooses the standard designation of $\hat{z}$ perpendicular on the plane.

Since the conduction in the degenerate Fermi system is realized only by states at the Fermi surface of wave vector k_F, p_x and p_z are expressed as a function of the polar angle $\varphi_{\mathbf{p}}$ between the momentum $\mathbf{p}$ and the [110] axis. In this case the Dresselhaus Hamiltonian obtains two distinct angular symmetries, effectively renormalizing the linear Dresselhaus strength to β [23,41,48]. We can now write the single particle Hamiltonian in terms of symmetric (+) and antisymmetric (−) combinations of the linear SO couplings, as

$$H_{\mathbf{p}} = \frac{\mathbf{p}^2}{2m^*} + \hbar(\mathbf{\Omega}_{\mathbf{p}} \times \sigma) \cdot \hat{y}. \quad (2)$$

The SO coupling is expressed via $\mathbf{\Omega}_{\mathbf{p}}$, which is defined as

$$\hbar\Omega^x_{\mathbf{p}} = k_F[(\alpha + \beta)\cos\varphi_{\mathbf{p}} - \beta_3 \cos 3\varphi_{\mathbf{p}}], \quad (3)$$

$$\hbar\Omega^z_{\mathbf{p}} = k_F[(\alpha - \beta)\sin\varphi_{\mathbf{p}} - \beta_3 \sin 3\varphi_{\mathbf{p}}], \quad (4)$$

where $\beta = \beta_1 - \beta_3$ is the renormalized linear Dresselhaus coefficient. We follow the standard formalism to calculate the quantum corrections to the conductivity [40,41,48,64] for the single particle Hamiltonian in Eq. (2).

The quantum corrections to the conductivity result from the renormalization of the scattering matrix element through the coherent superposition of the incident and scattered states. Although the bare impurity scattering is considered to be spin independent, in the presence of spin-orbit coupling, an additional spin component is involved in the calculated effective value of the matrix element. This is a result of the slight change in the energy of the electrons when the backscattered momentum is not perfectly antiparallel but rather deviates by a small vector $\mathbf{q}$. The ensuing variation in energy $\Delta E(\mathbf{q})$, considered small when compared with the energy uncertainty in the collision process $\hbar/\tau_0$, depends simultaneously on the two spin states of the electrons before and after the collision, which are considered uncorrelated. In a perturbative approach that involves a power expansion in $\Delta E(\mathbf{q})\tau_0/\hbar$, the renormalization is done through the eigenvalues of an operator, called the Cooperon, acting in the four-dimensional space associated with the two spin 1/2 particles. The eigenvalues of this operator then yield the corrections to the conductivity when summed over all the changes $\mathbf{q}$ and spin channels.

The possible total-spin states formed correspond either to total angular momentum $J = 0$, the singlet S, or to the total angular momentum $J = 1$, the triplet states T_0 and $T_\pm$, labeled after the values of $J_z = 0, \pm 1$. The associated four eigenvalues make up the quantum corrections in a system with SO coupling. The singlet is antisymmetric under the exchange of the incident and scattered spins, leading to an additional minus sign, thereby making the singlet contribution positive and, thus, responsible for the antilocalization contribution to the conductivity. The triplet states, on the other hand, are all symmetric and contribute negatively to the conductivity upon backscattering, thus making up the localization contribution to the conductivity.

If a magnetic field is applied, the electron energy is quantized in Landau levels (LL) of index n. In this case, the magnetoconductivity corrections are evaluated from a properly normalized sum that incorporates all the spin channels in all LL. The interplay between the Landau level quantization and the action of the SO coupling in determining the WL contribution in the $\alpha = \beta$ regime is illustrated in Fig. 1(a). For any given Landau level $|n\rangle$, we plot the energy of the orbit with respect to the singlet state and indicate the values of the Cooperon wave vector k_x along $\hat{x}$, which fixes the center of the orbit.

The coupling between the triplet modes decreases so much when $\alpha \simeq \beta$ that it can be considered independent in a first order approximation, as we show in the Appendix Eq. (A14). This is a consequence of the electron spins becoming polarized along the $\hat{z}$ direction under the action of an effective magnetic field $\sim(\alpha + \beta)$, an orientation that is left unchanged by the scattering process. In the vicinity of this high spin-symmetry point, the orbits of the triplet states are all separated in momentum space with T_+ located at $k_x - Q_+$, T_0 at k_x and T_- located at $k_x + Q_+$, where $Q_+ = \frac{2m^*}{\hbar^2}(\alpha + \beta)$. The energy of the orbits with the $T_\pm$ states is proportional to $((\alpha - \beta)^2 + 3\beta_3^2)/2$, while that of the state T_0 is proportional to $(\alpha - \beta)^2 + \beta_3^2$, as shown in Fig. 1(a). The four associated eigenstates are written in the tensor product space between the LL representation and the total angular momentum representation as $|n\rangle \bigotimes |J, J_z\rangle$. The corresponding Cooperon wave vector k_x is introduced in the position representation of $|n\rangle$.

Although the energies of the parallel spin modes $T_\pm$ are equal, the misalignment along k_x with the center orbits separated by exactly $2Q_+$ precludes any coupling between these modes. This situation corresponds to the separation in the momentum space of the two Fermi populations of up and down spin electrons by Q_+ that become spin polarized by an effective magnetic field proportional to $(\alpha + \beta)$ [27]. (The Cooperon is composed of two electrons, so the single particle states are separated in the momentum space by Q_+.) The remaining modes with $J_z = 0$, whose orbits are located at k_x, generate opposite sign contributions to WL. Exactly at $\alpha = \beta$ and $\beta_3 = 0$ they cancel, leading to the disappearance of the WAL. In Fig. 1(b) we illustrate how the states in the same Landau level evolve as a function of α/β for zero cubic term (full curves) and finite cubic term (dashed curves), which highlights the role played by the cubic Dresselhaus term, lifting the degeneracy at $\alpha = \beta$ such that the T_0 and S state no longer fully cancel, giving WAL even at $\alpha = \beta$.

In the Appendix, we outline the major steps for the calculation (with further details in the SM). Here, we give only the result of the closed-form expression for the conductivity correction $\Delta\sigma(B_\perp)$ in a magnetic field $B_\perp$, expressed in terms of the digamma function Ψ,

$$\begin{aligned}\Delta\sigma(B_\perp) = -\frac{e^2}{4\pi^2\hbar}\bigg[&\Psi\left(\frac{1}{2}+\frac{B_\varphi}{B_\perp}\right)+2\ln\frac{B_{\rm tr}}{B_\perp}\\ &-2\Psi\left(\frac{1}{2}+\frac{B_\varphi}{B_\perp}+\frac{B_{SO-}+3B_{SO3}}{2B_\perp}\right)\\ &-\Psi\left(\frac{1}{2}+\frac{B_\varphi}{B_\perp}+\frac{B_{SO-}+B_{SO3}}{B_\perp}\right)\bigg]. \qquad (5)\end{aligned}$$

The coherence time τ_φ and transport time $\tau_{\rm tr}$ define two characteristic fields, the dephasing field B_φ and the transport field $B_{\rm tr}$, which are given by

$$B_\varphi = \frac{\hbar}{4eD\tau_\varphi}, \qquad (6a)$$

$$B_{\rm tr} = \frac{\hbar}{4eD\tau_{\rm tr}}, \qquad (6b)$$

with D the diffusion constant in 2D.

The form of Eq. (5) is very similar to the one from Hikami, Larkin, and Nagaoka [38], but now the arguments in the digamma functions contain the linear Rashba and Dresselhaus terms as well as the cubic Dresselhaus term, via the effective magnetic fields $B_{\rm SO-}$ and $B_{\rm SO3}$. These are defined as

$$B_{\rm SO\pm} = \frac{\hbar}{4e}\left(\frac{2m^*}{\hbar^2}(\alpha\pm\beta)\right)^2, \qquad (7a)$$

$$B_{\rm SO3} = \frac{\hbar}{4e}\left(\frac{2m^*}{\hbar^2}\beta_3\sqrt{\frac{\tau_3}{\tau_1}}\right)^2, \qquad (7b)$$

where $\hbar$ the reduced Planck constant and e the elementary charge. The contribution of the cubic Dresselhaus term β_3 is represented in Eq. (7b), multiplied by the square root of the ratio of the backscattering time τ_1 and its third harmonic τ_3 which arises due to the higher angular harmonics of the Dresselhaus term in the SO Hamiltonian [41,48] [see Eq. (S4) in SM]. We note that Eq. (5) is valid for $B_{\rm SO+} \gg B_{\rm SO-}$ and thus is not valid for $\alpha = 0$ or $\beta = 0$, where the result of Refs. [41,48,49] applies, e.g., Eq. (37), in Ref. [49]. Further, when $\alpha = \beta = 0$, Eq. (39) in Ref. [49] results, with similar mathematical structure to Eq. (5) here, but Eq. (5) is not valid in this case.

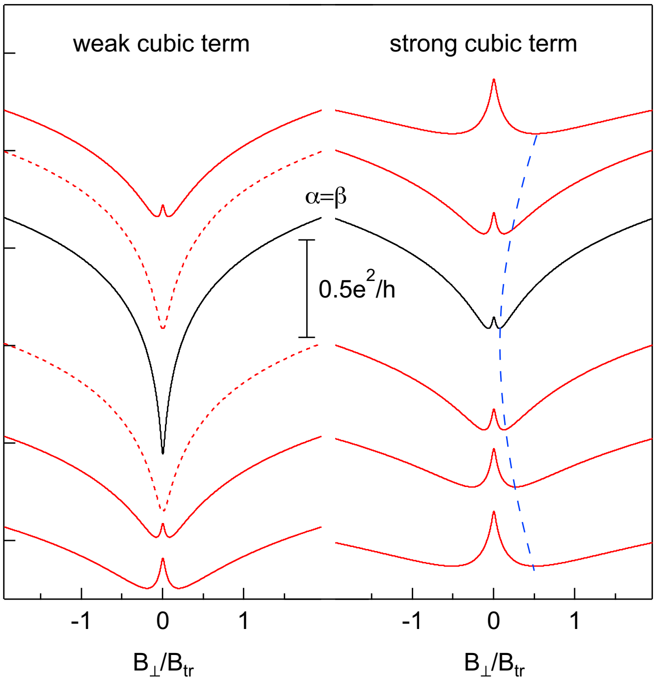

FIG. 2. Magnetoconductance curves in the regime close to the spin helix symmetry as given by Eq. (5). The black traces correspond to $\alpha = \beta$. Left panel: Spin orbit coupling causes a quench of the WL (dip less deep) before WAL appears (dashed red traces). Right panel: For a strong cubic term, WAL appears even at $\alpha = \beta$ and is defined by the WAL trace with the WAL minima closest to $B_\perp = 0$.

In modulation doped structures, the doping layer is set back from the 2D electron gas. Compared to doping incorporated inside the quantum well, this creates a softer, longer range scattering potential for the electrons with more prevalent small angle scattering [65,66]. For the ratio of scattering times, the range of possible values is $1/9 \leqslant \tau_3/\tau_1 \leqslant 1$, where 1/9 corresponds to dominant small angle scattering [49] and 1 indicates short range scattering (isotropic). Equation (5) is valid in the diffusive regime, where $B_\perp \ll B_{\rm tr}$ and naturally requires weak SO coupling. This is assuming that the spins are precessing only by a small angle in a time $\tau_{\rm tr}$, corresponding to the condition $B_{\rm SO\pm} \ll B_{\rm tr}$.

In Fig. 2 we plot the magnetoconductance according to Eq. (5) with and without the cubic Dresselhaus term. As we vary the Rashba strength α while keeping the renormalized Dresselhaus term β constant, the conductivity traces transition from WAL (red traces) to WL (black trace), where $\alpha = \beta$. We note that the absence of WAL alone (red dashed and black traces, left panel) does not uniquely identify the PSH symmetry point. Rather, the most pronounced WL curve (black trace) with the deepest and sharpest dip indicates realization of the PSH point. Some small amount of SO coupling (cubic and/or linear terms) away from the symmetry point quenches

WL, reducing the depth and sharpness of the WL dip without the appearance of WAL, i.e., a maximum of conductivity at zero field. A lower coherence time has a similar effect, also reducing the depth of the WL dip, and can be difficult to separate from the effects of weak SO coupling [67–69]. If a sufficiently strong cubic term is present, WL is suppressed and WAL appears even at $\alpha = \beta$ (black trace), where the position of the WAL minima (indicated by the dashed blue curve) are closest to $B_\perp = 0$.

III. EXPERIMENT

A. Control of spin orbit parameters

We will now discuss the different constituents of Eq. (7a) and Eq. (7b) and how they relate to experimental adjustable parameters. Electric fields, doping, and the interface of the heterojunction result in a confining potential, which causes structure inversion asymmetry and is the origin of the Rashba effect [24]. Its strength α can be tuned as a function of the electric field [16,17] and is parameterized in our QW as follows

$$\alpha = \alpha_0 + \alpha_1 \delta E_z, \tag{8}$$

where α_0 is a sample specific offset and α_1 accounts for the effect of the induced electric field detuning δE_z coming from the voltages applied to the top and back gates [see Eq. (A20) in the Appendix]. The Dresselhaus SO interaction [25] is characterized by the renormalized linear Dresselhaus strength β, which reads

$$\beta = \beta_1 - \beta_3 = \gamma\left(\langle k_z^2\rangle - \frac{k_F^2}{4}\right), \tag{9}$$

where $\beta_1 = \gamma\langle k_z^2\rangle$ and $\beta_3 = \frac{1}{4}\gamma k_F^2$ is the cubic Dresselhaus term, with γ being the bulk Dresselhaus material coefficient. As the Fermi momentum $k_F^2 = 2\pi n$ depends on the density n, the renormalized Dresselhaus strength becomes controllable via gate voltages, which has recently been demonstrated [23]. Over the range of the applied gate voltages $\langle k_z^2\rangle$ is effectively constant.

B. Evaluation procedure

In the experiment, we first extract the cubic term and phase coherence where the linear terms cancel but the cubic term already breaks spin symmetry. Then, we detune the linear terms away from equal size and can extract their strength as well, again from fits to the new theory. We control the strength of the SO parameters α and β with the top gate voltage V_T and the back gate voltage V_B. As described in the previous paragraphs, these parameters depend on density n and the detuning δE_z. To obtain a more useful parameter space, we measure the density as a function of V_T and V_B and obtain a density map, shown in Fig. 3, with contours of constant density, along which the detuning δE_z changes. We note that for sufficiently negative back gate and positive top gate voltages, the contours of constant density become nonlinear, which limits the usable range of δE_z and n. The range of the density is further limited by the requirement that the cubic Dresselhaus term β_3, which depends on density, be large enough, such that B_{SO3} causes WAL even at the PSH symmetry.

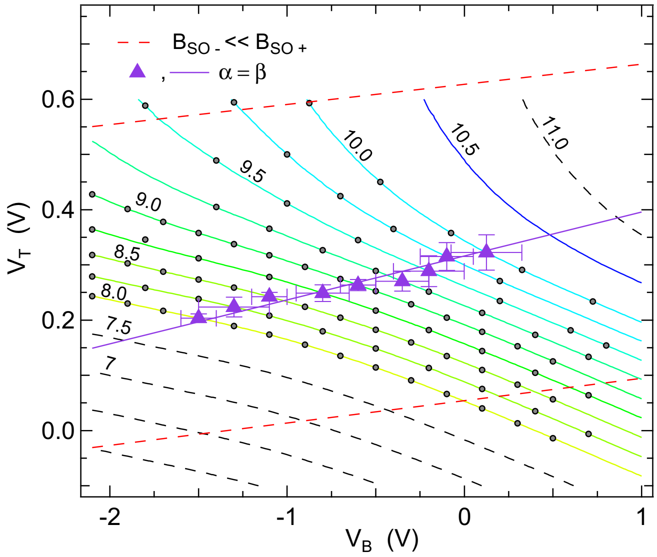

FIG. 3. Density map with symmetry points (purple triangles) as a function of top V_T and back gate V_B voltage for data set #2 (see SM [70] for details). Along contours of constant density (labeled in units of 10^{15} m^{-2}), B_{SO-} is changing as a function of detuning δE_z, while B_{SO3} is constant. The gray circles indicate the measured gate configurations. The triangles correspond to the approximate position where $\alpha = \beta$ and the purple line corresponds to a plot of the calculated PSH condition from the extracted SO parameters. Equation (5) is valid everywhere between the red dashed lines.

The PSH symmetry points are indicated by the purple markers in Fig. 3 and their position is estimated from the conductivity traces with the least pronounced WAL feature. This can be done, since along contours of constant density only $B_{\mathrm{SO}-}$ changes as a function of δE_z and B_{SO3} remains constant, as scattering potentials are thought to not change τ_3/τ_1 significantly for constant density. The gate configurations where conductivity traces were measured are indicated by the gray circles in Fig. 3. At the gate configurations around the symmetry point, $B_{\mathrm{SO}-}$ is very small and is set to zero when fitting Eq. (5) to the data, where only B_φ and B_{SO3} are the fit parameters (see Appendix Sec. D and Supplemental Material [70] Sec. III A). The transport field B_{tr} is known from independent Hall measurements of density n and mobility μ. Since the symmetry point is not precisely known, we determine B_{SO3} very similarly at the surrounding gate configurations and take the average value, thus obtaining a more robust value for B_{SO3}.

In Fig. 4(a), we show typical fits (red) to the measured (black) conductivity traces around the symmetry point. The agreement between fit and theory is very good for $B_\perp \ll B_{\mathrm{tr}}$, where B_{tr} is indicated by the dashed gray curve. The extracted fit parameters B_{SO3} (red triangles) and B_φ (blue triangles) are shown as a function of density in the upper panel of Fig. 4(b). A quadratic fit [see Eq. (7b)] to the B_{SO3} data finds good agreement, see red dashed line. At low temperatures, Nyquist dephasing dominates [71] and $\tau_\varphi^{-1} \propto T\lambda_F/l_e$, with T being the electron temperature, λ_F the Fermi wavelength, and l_e the mean free path. Here, the electron temperature is

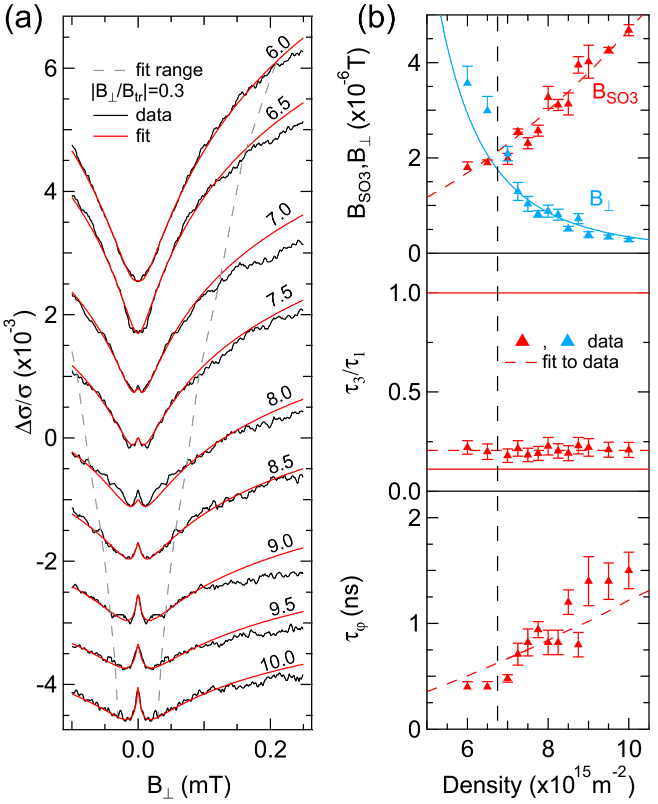

FIG. 4. (a) Measured conductivity traces (black) around the symmetry point and fits (red) using Eq. (5) with the respective density labeled at each trace in units of 10^{15} m^{-2}. The measured traces have been symmetrized in $B_\perp$ for fitting. The gray dashed curves correspond to the fit range obeying $B_\perp \ll B_{\mathrm{tr}}$. (b) Upper panel: extracted B_{SO3} values versus density. The red dashed curve is a quadratic fit to B_{SO3}. The blue markers and curve correspond to the extracted and calculated B_φ (see main text). Middle panel: extracted τ_3/τ_1 using the later to be determined γ for each individual value of B_{SO3} from the upper panel. The red dashed line is the average of τ_3/τ_1. Lower panel: coherence time from the extracted B_φ for the respective density and mobility. The red dashed curve is a fit to the data assuming Nyquist dephasing. For the two lowest densities 6.0 and 6.5 (left of the dashed vertical line), the extracted values of B_{SO3} and B_φ are only bounds, see text.

$\sim$100 mK estimated independently [72,73]. Since $B_\varphi \propto \tau_\varphi^{-1}$, we can express B_φ in terms of density and mobility via the above expression for τ_φ. This is shown with the blue curve, reproducing the trend of the extracted B_φ quite well. For $n < 7 \times 10^{15}$ cm^{-2}, indicated by the dashed black line in Fig. 4(b), we observe that the conductivity traces in Fig. 4(a) no longer show a WAL feature and that $B_{\mathrm{SO3}} \leqslant B_\varphi$. Thus for densities to the left of the black dashed line, the extraction of a meaningful value for B_{SO3} and B_φ is no longer possible and only an upper bound can be determined.

Using the value of B_φ, we can also determine the coherence time τ_φ for each density, which is shown in the lower panel of Fig. 4(b). The coherence time is of the order of 1 ns, which is a value expected in GaAs 2D electron gases at mK temperatures [54,74,75]. The red dashed curve shows the dependence of τ_φ on density, calculated also for Nyquist dephasing, in qualitative agreement with the data. This allows us to keep τ_φ constant along contours of constant density as the mobility change of $\sim$10% is smaller than the error on τ_φ.

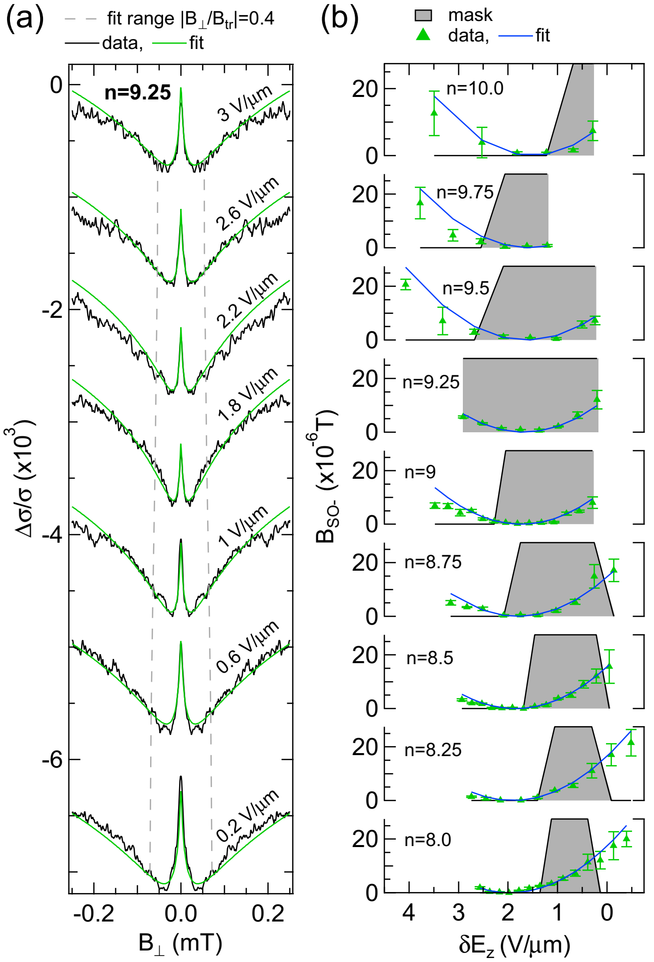

FIG. 5. Measured traces away from $\alpha \approx \beta$. (a) Fits (green) to the conductivity traces (black) for constant density $n = 9.25 \times 10^{15}$ m^{-2} in Fig. 3. The gray dashed lines indicate the range for the diffusive approximation. Each curve is labeled with its detuning value δE_z. (b) Extracted values of $B_{\mathrm{SO}-}$ versus the detuning δE_z for all densities (arranged vertically and labeled in units of 10^{15} m^{-2} for each $B_{\mathrm{SO}-}$ curve). The error bars correspond to the error on the fit parameter (i.e., one standard deviation). The data in the gray shaded area is included in the fit.

We now proceed with the evaluation away from the PSH symmetry by keeping B_{SO3} and τ_φ fixed for each density, thus facilitating the extraction of $B_{\mathrm{SO}-}$ as a function of the detuning δE_z. In Fig. 5(a) we show the fits (green) to the conductivity traces along constant density, finding good agreement of the fit with the data. We repeat this for all densities with the respective values of τ_φ and B_{SO3} as previously determined. This delivers a full data set of $B_{\mathrm{SO}-}$ as a function of the density n and the detuning δE_z. Rewriting Eq. (7a) with the expressions of α and β [see Eq. (8) and Eq. (9)] we obtain

$$B_{\mathrm{SO}-} \propto \left(A + \alpha_1 \delta E_z + \frac{1}{2}\pi\gamma n\right)^2, \qquad (10)$$

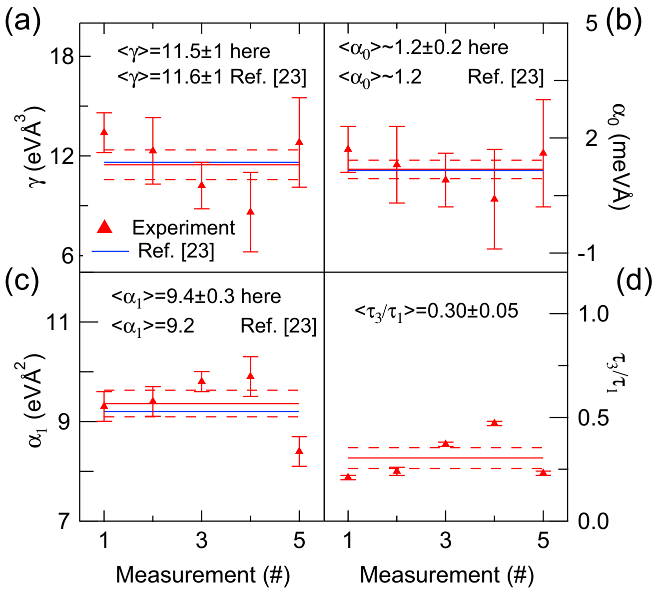

FIG. 6. SO parameters from five measurements obtained on two samples. Measurements 1 and 3 correspond to Hall bar no. I and measurements 2, 4, and 5 correspond to Hall bar no. II, where measurement 5 is from another cool down, details in SM [70] Sec. II. The blue lines correspond to the values obtained in a previous work [23], the red lines correspond to their average, and the red dashed lines correspond to the standard deviation of the mean. (a) Dresselhaus coefficient γ (b) offset α_0 of the Rashba parameter, (c) α_1 of the Rashba parameter and (d) average scattering time ratio τ_3/τ_1.

with the fit parameters α_1 and γ and $A = \alpha_0 - \gamma\langle k_z^2\rangle$. Thus, the extracted values of $B_{\mathrm{SO}-}$ are expected to follow a parabolic shape, which is also seen in Fig. 5(b). Some deviations from a parabola are apparent, which are due to the nonlinear dependence of the density on gate voltages (see Fig. 3). We exclude such data from the fit. The gray shaded area indicates the data points included in the fit—the fit mask—considering the validity of the theory and using only the linear region of gate voltage parameter space, see Fig. 3 and Appendix Sec. E. The nonlinear behavior can be seen for larger detunings as the effect of δE_z weakens and the $B_{\mathrm{SO}-}$ parabolas become stretched.

The resulting fit to the data is shown in Fig. 5(b) (blue curve), in good agreement with the data within the fit mask and directly yields A, α_1, and γ. Self consistent simulations give a value for $\langle k_z^2\rangle$ [23], allowing us to determine the Rashba offset parameter α_0 from A.

C. Determination of the SO parameters

In Fig. 6 we show the results from five independent measurements obtained from 2 Hall bar samples on the same quantum well material (see SM [70] Sec. II). Panels (a) through (c) show the fitted values for γ, α_0, and α_1, with their average (red lines) and standard deviation of the mean (red dashed lines). Data sets vary in exact position and especially in number of points measured per density, resulting in varying fit values and associated error bars. To work from the largest possible set of data available we simply include all these independent measurements in the analysis. The complete data sets can be seen on display in the SM [70]. The blue lines correspond to the respective values obtained recently from the same wafer material in a previous study [23] with a different method.

We note that the reported values of γ in quantum transport over the last 30 years ranged from ~4–28 eV Å^3 [54,76]. The values of $\gamma = 28$ eV Å^3 are close to the literature value, which is obtained from $\mathbf{k}\cdot\mathbf{p}$ calculations. However, electronic band-structure calculations in $\mathbf{k}\cdot\mathbf{p}$ approximation or with density functional theory tend to give inaccurate SO parameters because these calculations neglect either the many body interactions or contain too many parameters which have to be assumed. In recent years, self consistent numerical calculations including the cubic Dresselhaus term were combined with experiments [23,43], giving values $\gamma \sim 9$–11.5 eV Å^3. These results are confirmed by state of the art single particle *GW* approximations, calculating the self-energy of a many body system of electrons [77] or density functional theory with density dependent exchange potentials [78]. These results agree very well with our average of 11.5 ± 1 eVÅ^3 and also recent works using optical spin excitation [34,42,44].

The offset parameter α_0 accounts for SO coupling from the electric fields of the charges in the doping layer and the potential of the Hartree term and is a sample specific parameter. It can be calculated via self-consistent methods [23,61,79], which is identical with the average of the extracted value. Finally, the Rashba field parameter α_1 has an average value of around 9.4 eV Å^2 which can also be calculated purely from band structure parameters in a quantum well [79] giving 9.2 eV Å^2, very close to previously extracted values [23] and ours.

With the previously determined values of B_{SO3}, we can now extract the value of τ_3/τ_1 using Eq. (7b) and the now known value of γ. Assuming τ_3/τ_1 being constant over the range of measured densities, allows us to extract τ_3/τ_1 from the quadratic fit to the B_{SO3} data, shown in the upper panel of Fig. 4(b). The fit parameter is proportional to $\gamma\tau_3/\tau_1$ and turns out to be almost the same for all measurements and yields the values shown in Fig. 6(d) by supplying the respective value of γ from each measurement. Since $\tau_3/\tau_1 \propto 1/\gamma^2$, smaller values of γ yield a larger τ_3/τ_1, see data points #3 and #4 in Fig. 6(d). From the $B_{\mathrm{SO3}}(n)$ data we can also determine τ_3/τ_1 as a function of density n, using the extracted γ, which is shown in the middle panel of Fig. 4(b). The values barely change over the range of measured densities and its average value of ~0.2 agrees with the one extracted from the fit to B_{SO3}. Overall, the extracted values of τ_3/τ_1 are around 0.3, much smaller than 1, indicating that small angle scattering dominates [49], as expected for a modulation doped structure.

IV. CONCLUSION

By introducing a new in-plane spin quantization axis at the PSH symmetry point, we notice the full decoupling of the Landau levels and, to lowest order, the triplets of the Cooperon modes also become fully independent. This elegantly simplifies the calculation and provides a simple, closed-form expression for the quantum corrections in the vicinity of the PSH symmetry $\alpha = \beta$, which includes the Rashba and linear

Dresselhaus terms, as well as the cubic Dresselhaus term. The calculation fully accounts for Landau level quantization and provides a new paradigm of localization in the weakly broken spin symmetry regime. We test the new expression against experiment and find excellent agreement. Further, we have studied how breaking of the PSH symmetry by a slight mismatch of the linear terms or by the cubic term allows to quantify the various SO parameters in a GaAs QW. We directly obtain fundamental SO parameters such as the Dresselhaus coefficient γ and the Rashba parameter α_1, which are in good agreement with recent calculations and experiments.

The good agreement of the extracted SO parameters based on this theory with results obtained in Ref. [23] is an excellent indicator that the new model accurately describes the quantum corrections in the vicinity of the PSH symmetry and can be used as a tool in future studies, whenever Rashba and Dresselhaus SO strengths are comparable. Moreover, when the SO parameters extracted here are employed in the general solution given in Ref. [63], experimental data obtained for $\alpha/\beta \in [0, 0.5]$ is matched with remarkable accuracy. The capability to extract all relevant SO parameters from quantum transport experiments—obtained from fits to closed-form expressions—opens the door to engineer and control the SO interaction as a useful resource in novel quantum materials such as tailored spin textures, Majorana fermions, and parafermions. Further, it can be used to coherently manipulate spins in emerging quantum technologies such as spintronics and quantum computation. This technique is also applicable in other materials where the symmetry-broken PSH regime is accessible.

ACKNOWLEDGMENTS

We would like to thank S. Hoffman, M. Kohda, K. Richter, and G. Salis for valuable inputs and stimulating discussions, and M. Steinacher for technical support. This work was supported by the Swiss Nanoscience Institute (SNI), NCCR QSIT, Swiss NSF, ERC starting grant (DMZ), the EU H2020 European Microkelvin Platform EMP, Grant No. 824109, US NSF DMR-1306300, NSF MRSEC DMR-1420709, the follow on program of the UCSB Kavli Institute under NSF PHY-1748958, and ONR N00014-15-1-2369, Brazilian Grants No. 2016/08468-0 and No. 2016/50200-4 (SPRINT program), São Paulo Research Foundation (FAPESP), CNPq, PRP/USP (Q-NANO), and China NSF 11004120 and 11874236. P.J.W., J.C.E., and D.M.Z. designed the experiment and analyzed the data. All authors discussed the results and commented on the manuscript. S.M. and D.D.A. designed, simulated, and carried out the molecular beam epitaxy growth of the heterostructure. P.J.W. carried out the measurements, D.C.M. derived the new expression for the quantum corrections, F.D. fabricated the samples, J.F. and J.C.E. developed and carried out the simulations and theoretical work.

P.J.W. and D.C.M. contributed equally to this work.

APPENDIX: APPENDIX: MATERIALS AND METHODS

1. Formalism to calculate quantum corrections

Here, we highlight the most relevant results from the formalism to calculate the quantum corrections. The full procedure to calculate the Cooperon and its eigenvalues is shown in detail in the Supplemental Material (SM) [70]. Our starting point is the general expression connecting the quantum corrections to the conductivity $\Delta\sigma$ and the Cooperon eigenvalues $C_i(\mathbf{q})$,

$$\Delta\sigma = -\frac{2e^2 D\tau_0^2\nu_0}{\hbar^2}\sum_{\mathbf{q},i} C_i(\mathbf{q})\,. \tag{A1}$$

To determine the relevant singlet and triplet Cooperon modes ($i = 0, 1, 2, 3$), we start with the impurity mediated equation for the Cooperon amplitude $C_{\mathbf{p},\mathbf{p}'}(\mathbf{q})$

$$C_{\mathbf{p},\mathbf{p}'}(\mathbf{q}) = |V_{\mathbf{p},\mathbf{p}'}|^2 + \sum_{\mathbf{p}''} |V_{\mathbf{p},\mathbf{p}''}|^2 G^+_{-\mathbf{p}''+\hbar\mathbf{q},\epsilon+\hbar\omega} G^-_{\mathbf{p}'',\epsilon} C_{\mathbf{p}'',\mathbf{p}'}\,. \tag{A2}$$

The Cooperon amplitude above represents the effective interaction vertex which renormalizes the impurity scattering potential $V_{\mathbf{p},\mathbf{p}'}$. It iteratively includes all higher-order processes (multiple scattering events) involving the scattering off of impurities of two electrons following time-reversed paths described by the retarded and advanced impurity-averaged propagators $G^\pm$. We solve Eq. (A2) via an iterative procedure by expanding the Cooperon amplitude in its angular harmonics and in the limit $\hbar q \ll p$ (since $\hbar\mathbf{q} = \mathbf{p} + \mathbf{p}'$ and $\mathbf{p}' \approx -\mathbf{p}$). After some lengthy but straightforward calculation (SM) we find for the relevant zeroth-order harmonic of the Cooperon amplitude

$$C^{(0)}_{\mathbf{p},\mathbf{p}'}(\mathbf{q}) = \frac{|V_{\mathbf{p},\mathbf{p}'}|^2}{\tau_0\mathcal{H}}\,. \tag{A3}$$

The operator $\mathcal{H}$ in the denominator of the Cooperon is

$$\begin{aligned}\mathcal{H} = Dq^2 + \frac{1}{\tau_\varphi} + D\big\{&\big[Q_+^2 + Q_3^2\big]J_z^2 + \big[Q_-^2 + Q_3^2\big]J_x^2\\ &+ 2Q_+q_zJ_x - 2Q_-q_xJ_z\big\},\end{aligned} \tag{A4}$$

where $J_{x,z}$ are the total spin angular momentum components and

$$Q_\pm = \frac{2m^*}{\hbar^2}(\alpha \pm \beta), \tag{A5}$$

$$Q_3 = \frac{2m^*}{\hbar^2}\left(\beta_3\sqrt{\frac{\tau_3}{\tau_1}}\right). \tag{A6}$$

We can now diagonalize the Cooperon operator in Eq. (A3), a matrix in the basis of the total angular momentum of the two spins, and obtain the quantum correction from Eq. (A1). In what follows, we carry out this procedure for the case in the presence of a quantizing magnetic field $B_\perp$ relevant for the experimental probing of the weak- (and anti-) localization corrections to the conductivity. As described in detail in the SM, in this case we need to switch to a real space description. This is so because in the presence of a magnetic field we approximate the propagators by simply multiplying their zero-field counterpart by a vector potential ($\mathbf{A}$) dependent phase [40]

$$\tilde{G}^\pm(\mathbf{r},\mathbf{r}') = e^{\frac{ie}{\hbar}\int_{\mathbf{r}}^{\mathbf{r}'}\mathbf{A}(\mathbf{l})\cdot d\mathbf{l}}\,G^\pm(\mathbf{r},\mathbf{r}')\,. \tag{A7}$$

This standard procedure leads to the change $\mathcal{H} \rightarrow \tilde{\mathcal{H}}$ with

$$\tilde{\mathcal{H}}(\mathbf{r}, \mathbf{r}') = e^{i\frac{2e}{\hbar}\int_{\mathbf{r}}^{\mathbf{r}'}\mathbf{A}(\mathbf{l})\cdot d\mathbf{l}}\mathcal{H}(\mathbf{r}, \mathbf{r}'), \tag{A8}$$

in the denominator of the zeroth-order Cooperon operator; the Fourier transform of $\mathcal{H}(\mathbf{r}, \mathbf{r}')$ at zero magnetic field is given by Eq. (A4).

We solve the generalized eigenvalue problem,

$$\int e^{i\frac{2e}{\hbar}\mathbf{A}\cdot(\mathbf{r}'-\mathbf{r})}\mathcal{H}(\mathbf{r}, \mathbf{r}')\psi(\mathbf{r}')d\mathbf{r}' = \mathcal{E}\psi(\mathbf{r}), \tag{A9}$$

with suitable expansions of the integrand in powers of $\Delta\mathbf{r} = \mathbf{r}' - \mathbf{r} \ll l$ and define the canonical transformation,

$$-i\nabla_z = \sqrt{\frac{2eB_\perp}{\hbar}}\frac{(a - a^\dagger)}{i\sqrt{2}}, \tag{A10}$$

$$z + z_0 = \frac{1}{\sqrt{\frac{2eB_\perp}{\hbar}}}\frac{(a + a^\dagger)}{\sqrt{2}}, \tag{A11}$$

with $z_0 = k_x\hbar/2eB_\perp$ (k_x is the Cooperon wave vector along $\hat{x}$). a and $a^\dagger$ are bosonic operators, i.e., $[a, a^\dagger] = 1$ that describe the quantization of the Landau levels. We thus obtain the characteristic equation in the number representation,

$$\begin{aligned}\Bigg\{\frac{1}{\tau_\varphi} &+ D\left(Q_+^2 + Q_3^2\right)J_z^2 + \left(Q_-^2 + Q_3^2\right)J_x^2 \\ &- DQ_+J_z\sqrt{\frac{4eB_\perp}{\hbar}}(a + a^\dagger) - iDQ_-J_x\sqrt{\frac{4eB_\perp}{\hbar}}(a - a^\dagger) \\ &+ D\left(\frac{4eB_\perp}{\hbar}\right)\left(a^\dagger a + \frac{1}{2}\right)\Bigg\}|u\rangle = \mathcal{E}|u\rangle,\end{aligned} \tag{A12}$$

where $|u\rangle$ is the corresponding eigenket.

In the basis of the total spin angular momentum associated with the four-dimensional tensor product of the two spin operators of the electrons in time-reversed path, we evaluate the singlet and triplet Landau eigenvalues $\tilde{\mathcal{E}}_{n,i} = \mathcal{E}_{n,i}/(4DeB_\perp/\hbar)$ of the Cooperon ($i = 0$ corresponds to the singlet state and $i = 1, 2, 3$ label the triplet state).

The singlet $J = 0, J_z = 0$ solution of the Cooperon equation is immediately factored, as it is diagonal both in the spin and Landau level spaces. With these, the single Cooperon mode generates an eigenvalue for the nth Landau level given by

$$\tilde{\mathcal{E}}_{n,0} = n + \frac{1}{2} + \frac{B_\varphi}{B_\perp}. \tag{A13}$$

The remaining triplet equation, from Eq. (A12), is written in the basis of $J = 1, J_z = \{1, 0, 1\}$ in terms of the effective magnetic fields from Eqs. (6a)–(7b) as

$$\begin{vmatrix} \begin{array}{c}\frac{B_\varphi}{B_\perp} + \frac{B_{\mathrm{SO}+}}{B_\perp} + \frac{B_{\mathrm{SO}-}+3B_{\mathrm{SO}3}}{2B_\perp} \\ +a^\dagger a + \frac{1}{2} - \sqrt{\frac{B_{\mathrm{SO}+}}{B_\perp}}(a + a^\dagger) - \tilde{\mathcal{E}}\end{array} & -i\sqrt{\frac{B_{\mathrm{SO}-}}{2B_\perp}}(a - a^\dagger) & \frac{B_{\mathrm{SO}-}+B_{\mathrm{SO}3}}{2B_\perp} \\ -i\sqrt{\frac{B_{\mathrm{SO}-}}{2B_\perp}}(a - a^\dagger) & \frac{B_\varphi}{B_\perp} + \frac{B_{\mathrm{SO}-}+B_{\mathrm{SO}3}}{B_\perp} + a^\dagger a + \frac{1}{2} - \tilde{\mathcal{E}} & -i\sqrt{\frac{B_{\mathrm{SO}-}}{2B_\perp}}(a - a^\dagger) \\ \frac{B_{\mathrm{SO}-}+B_{\mathrm{SO}3}}{2B_\perp} & -i\sqrt{\frac{B_{\mathrm{SO}-}}{2B_\perp}}(a - a^\dagger) & \begin{array}{c}\frac{B_\varphi}{B_\perp} + \frac{B_{\mathrm{SO}+}}{B_\perp} + \frac{B_{\mathrm{SO}-}+3B_{\mathrm{SO}3}}{2B_\perp} \\ +a^\dagger a + \frac{1}{2} + \sqrt{\frac{B_{\mathrm{SO}+}}{B_\perp}}(a + a^\dagger) - \tilde{\mathcal{E}}\end{array} \end{vmatrix} = 0. \tag{A14}$$

In the limit of $\alpha \approx \beta$, $B_{\mathrm{SO}-} \ll B_{\mathrm{SO}+}$, as well as $B_{\mathrm{SO}3} \ll B_{\mathrm{SO}+}$, leading to a justified cancellation of all off-diagonal terms proportional with $B_{\mathrm{SO}-}$ or $B_{\mathrm{SO}-} + B_{\mathrm{SO}3}$ in Eq. (A14). Then, by redefining the canonical transformations to operators $a, a^\dagger$ are modified to incorporate the additional translation proportional to Q_+,

$$\begin{aligned} -i\nabla_z &= \sqrt{\frac{2eB_\perp}{\hbar}}\frac{(a - a^\dagger)}{i\sqrt{2}}, \\ z + z_0 \mp \frac{\hbar Q_+}{2eB_\perp} &= \frac{1}{\sqrt{\frac{2eB_\perp}{\hbar}}}\frac{(a + a^\dagger)}{\sqrt{2}}, \end{aligned} \tag{A15}$$

where $-$ corresponds to $J_z = 1$ and $+$ to $J_z = -1$. Then each mode can be diagonalized independently generating the following triplet eigenvalues,

$$\tilde{\mathcal{E}}_{n,1} = \tilde{\mathcal{E}}_{n,2} = n + \frac{1}{2} + \frac{B_\varphi}{B_\perp} + \frac{B_{SO-} + 3B_{SO3}}{2B_\perp}, \tag{A16}$$

$$\tilde{\mathcal{E}}_{n,3} = n + \frac{1}{2} + \frac{B_\varphi}{B_\perp} + \frac{B_{SO-} + B_{SO3}}{B_\perp}. \tag{A17}$$

Within the same approximation, the associated eigenstates are written in the tensor product space between the LL and the total angular momentum representations as $|n\rangle \bigotimes |J, J_z\rangle$. Because the modes are obtained from three different canonical transformations, Eq. (A11) for $J_z = 0$, and Eq. (A15) for $J_z = \pm 1$, the corresponding orbit center in the position representation is determined by the Cooperon wave vector k_x for $J_z = 0$ and $k_x \mp Q_+$ for $J_z = \pm 1$, respectively. The difference $2Q_+$ between the centers of the parallel-spin Cooperon configurations corresponds to the Q_+ separation between the k_x momenta of the single-particle states associated with the $\alpha = \beta$ regime [27]. (The Cooperon has a charge $2e$ vs the single particle states of charge e, hence the halving of the momentum translation along $\hat{x}$.)

Phenomenologically, this situation corresponds to a decreased coupling between the triplet modes within the same Landau level as the scattering processes do not involve any spin flipping. The original orientation of the incident particle is preserved as the electron population becomes polarized by the effective field $B_{\mathrm{SO}+}$ along the $\hat{z}$ axis.

After angular integration, Eq. (A1) is properly modified to account for the magnetic field, i.e., $\frac{1}{2\pi}\int q dq \to \frac{1}{4\pi}\frac{4eB_\perp}{\hbar}\sum_n$, and the quantum corrections to the conductivity $\Delta\sigma(B_\perp)$ in the presence of a magnetic field are obtained,

$$\begin{aligned} \Delta\sigma(B_\perp) &\sim -\sum_{n=0}^{n_m}\sum_{i=0,3}\frac{1}{\tilde{\mathcal{E}}_{n,i}} \\ &= \sum_{n=0}^{n_m}\left\{\frac{2}{n+\frac{1}{2}+\frac{B_\varphi}{B_\perp}+\frac{B_{SO-}+3B_{SO3}}{2B_\perp}}\right. \\ &\quad \left. +\frac{1}{n+\frac{1}{2}+\frac{B_\varphi}{B_\perp}+\frac{B_{SO-}+B_{SO3}}{B_\perp}}-\frac{1}{n+\frac{1}{2}+\frac{B_\varphi}{B_\perp}}\right\}. \end{aligned} \tag{A18}$$

By using the general identity

$$\begin{aligned} \sum_{n=0}^{n_m}\frac{1}{n+a} &= \sum_{n=0}^{n_m}\frac{1}{n+a}-\sum_{n=1}^{n_m}\frac{1}{n}+\sum_{n=1}^{n_m}\frac{1}{n} \\ &= -\sum_{n=1}^{n_m}\frac{a-1}{n(n+a-1)}+C+\ln n_m \\ &= -\Psi(a)+\ln n_m, \end{aligned} \tag{A19}$$

(C is the Euler constant), we obtain Eq. (5). This is the main theoretical result of our work and essential for the two-stage fitting procedure used to accurately determine all the spin-orbit couplings presented here. We emphasize that the closed form expression for $\Delta\sigma(B_\perp)$ in Eq. (5) contains not only the Rashba but also the linear and cubic Dresselhaus terms.

2. GaAs Quantum Well Materials

The sample is a modulation-doped 11-nm-thick GaAs/AlGaAs quantum well, grown by molecular beam epitaxy on a (001) n-doped substrate with two symmetrically placed δ doping layers, each set back 12 nm from the quantum well. The highly n-doped substrate serves as a back gate by incorporating a 600-nm-thick low temperature grown GaAs barrier, which pins the Fermi level midgap [80]. This reduces the effective distance d_B from the QW to the back gate and increases the available range of gate voltages. Using wet etching, two identical Hall bars were defined with a Ti/Au gate of 300 × 100 μm^2 on top. The 2DEG is contacted with thermally annealed low resistance GeAu/Pt contacts. The annealing parameters were carefully determined to achieve decent contact to the 2D gas without short circuiting the back gate. The top and back gate architecture allows us to keep the density in the QW constant, while changing the electric field detuning δE_z, which can be calculated in terms of the distances effective d_T and d_B and gate voltages V_T and V_B of the top and back gate, using a simple plate capacitor model. The detuning then reads [23]:

$$\delta E_z = \frac{1}{2}\left(\frac{V_T}{d_T}-\frac{V_B}{d_B}\right). \tag{A20}$$

The back gate range is $[-3, 1]$ V and $[-0.3, 0.6]$ V for the top gate, corresponding to a density range of [3,12] $\times 10^{15}$ m^{-2} and mobility range [2,14] m^2/Vs. Individual density and mobility maps are shown in the SM [70].

3. Measurement Technique

We perform the experiments in a ^{3}He-^{4}He dilution refrigerator with a base temperature of 20 mK. We measure in a standard four-wire lock-in configuration with a time constant of 100 ms and a current bias of 100 nA, chosen to avoid self-heating, which can reduce the coherent part of the signal. After setting the gate voltages for each gate configuration gates were given 20 minutes to stabilize. To observe a clear WL/WAL signal each trace was measured at least 10–20 times and averaged.

4. Symmetry Point Determination and Value of B_{SO3}

To obtain a value of B_{SO3}, the symmetry point (i.e., $\alpha = \beta$) has to be determined first. For this we perform fits to the measured conductivity traces for all gate configurations along constant density but replace the SO fields in the argument of Eq. (5) with $B^*_{\mathrm{SO}} \propto (\alpha-\beta)^2 + B_{\mathrm{SO3}}$ and the extracted value of B^*_{SO} will show a minima at $\alpha = \beta$ and we can locate the approximate position of the symmetry point for each density, where we can then estimate the value of B_{SO3} (see SM [70], Sec. III).

5. Fit Mask

The fit mask ensures that the data points included are described by Eq. (5) and have the correct δE_z. We exclude data from the gate configurations in the nonlinear region of the density map (see Fig. 3), where the contours for $V_B \lesssim -1$V, start to bend. This bending corresponds to a change in the effective distance d_B to the back gate, which we use to calculate the detuning δE_z. We suspect unpinning of the Fermi level to be the reason for this change in d_B. For more positive gate voltages we exclude data from gate configurations, where the fit to the conductivity traces no longer matches the data. This gives a lower bound on the validity of Eq. (5) and agrees quite well with the condition $B_{SO-} \ll B_{SO+}$ (see red dashed lines in Fig. 3).

[1] J. Schliemann, Colloquium: Persistent spin textures in semiconductor nanostructures, Rev. Mod. Phys. **89**, 011001 (2017).

[2] M. Kohda and G. Salis, Physics and application of persistent spin helix state in semiconductor heterostructures, Semicond. Sci. Technol. **32**, 073002 (2017).

[3] Y. K. Kato, R. C. Myers, A. C. Gossard, and D. D. Awschalom, Observation of the spin Hall effect in semiconductors, Science **306**, 1910 (2004).

[4] J. Sinova, D. Culcer, Q. Niu, N. A. Sinitsyn, T. Jungwirth, and A. H. MacDonald, Universal Intrinsic Spin Hall Effect, Phys. Rev. Lett. **92**, 126603 (2004).

[5] B. A. Bernevig, T. L. Hughes, and S.-C. Zhang, Quantum spin hall effect and topological phase transition in HgTe quantum wells, Science **314**, 1757 (2006).

[6] M. König, S. Wiedmann, C. Brüne, A. Roth, H. Buhmann, L. W. Molenkamp, X.-L. Qi, and S.-C. Zhang, Quantum spin hall insulator state in HgTe quantum wells, Science **318**, 766 (2007).

[7] C. Liu, T. L. Hughes, X.-L. Qi, K. Wang, and S.-C. Zhang, Quantum Spin Hall Effect in Inverted Type-II Semiconductors, Phys. Rev. Lett. **100**, 236601 (2008).

[8] I. Knez, R.-R. Du, and G. Sullivan, Evidence for Helical Edge Modes in Inverted InAs/GaSb Quantum Wells, Phys. Rev. Lett. **107**, 136603 (2011).

[9] R. M. Lutchyn, J. D. Sau, and S. Das Sarma, Majorana Fermions and a Topological Phase Transition in Semiconductor-Superconductor Heterostructures, Phys. Rev. Lett. **105**, 077001 (2010).

[10] Y. Oreg, G. Refael, and F. von Oppen, Helical Liquids and Majorana Bound States in Quantum Wires, Phys. Rev. Lett. **105**, 177002 (2010).

[11] I. Žutić, J. Fabian, and S. Das Sarma, Spintronics: Fundamentals and applications, Rev. Mod. Phys. **76**, 323 (2004).

[12] D. Awschalom, N. Samarth, and D. Loss, *Semiconductor spintronics and quantum computation* (Springer, Berlin, London, 2011).

[13] D. Loss and D. P. DiVincenzo, Quantum computation with quantum dots, Phys. Rev. A **57**, 120 (1998).

[14] R. Hanson, L. P. Kouwenhoven, J. R. Petta, S. Tarucha, and L. M. K. Vandersypen, Spins in few-electron quantum dots, Rev. Mod. Phys. **79**, 1217 (2007).

[15] C. Kloeffel and D. Loss, Prospects for spin-based quantum computing in quantum dots, Annu. Rev. Condens. Matter Phys. **4**, 51 (2013).

[16] G. Engels, J. Lange, T. Schäpers, and H. Lüth, Experimental and theoretical approach to spin splitting in modulation-doped $In_xGa_{1-x}As$/InP quantum wells for $B \to 0$, Phys. Rev. B **55**, R1958(R) (1997).

[17] J. Nitta, T. Akazaki, H. Takayanagi, and T. Enoki, Gate Control of Spin-Orbit Interaction in an Inverted $In_{0.53}Ga_{0.47}As/In_{0.52}Al_{0.48}As$ Heterostructure, Phys. Rev. Lett. **78**, 1335 (1997).

[18] S. J. Papadakis, E. P. D. Poortere, H. C. Manoharan, M. Shayegan, and R. Winkler, The effect of spin splitting on the metallic behavior of a two-dimensional system, Science **283**, 2056 (1999).

[19] D. Grundler, Large Rashba Splitting in InAs Quantum Wells due to Electron Wave Function Penetration into the Barrier Layers, Phys. Rev. Lett. **84**, 6074 (2000).

[20] T. Koga, J. Nitta, T. Akazaki, and H. Takayanagi, Rashba Spin-Orbit Coupling Probed by the Weak Antilocalization Analysis in InAlAs/InGaAs/InAlAs Quantum Wells as a Function of Quantum Well Asymmetry, Phys. Rev. Lett. **89**, 046801 (2002).

[21] M. Kohda, V. Lechner, Y. Kunihashi, T. Dollinger, P. Olbrich, C. Schönhuber, I. Caspers, V. V. Bel'kov, L. E. Golub, D. Weiss, K. Richter, J. Nitta, and S. D. Ganichev, Gate-controlled persistent spin helix state in (In,Ga)As quantum wells, Phys. Rev. B **86**, 081306(R) (2012).

[22] K. Yoshizumi, A. Sasaki, M. Kohda, and J. Nitta, Gate-controlled switching between persistent and inverse persistent spin helix states, Appl. Phys. Lett. **108**, 132402 (2016).

[23] F. Dettwiler, J. Fu, S. Mack, P. J. Weigele, J. C. Egues, D. D. Awschalom, and D. M. Zumbühl, Stretchable Persistent Spin Helices in GaAs Quantum Wells, Phys. Rev. X **7**, 031010 (2017).

[24] Y. Bychkov and E. Rashba, Properties of a 2D electron gas with lifted spectral density, JETP Lett. **39**, 78 (1984).

[25] G. Dresselhaus, Spin-orbit coupling effects in zinc blende structures, Phys. Rev. **100**, 580 (1955).

[26] J. Schliemann, J. C. Egues, and D. Loss, Nonballistic Spin-Field-Effect Transistor, Phys. Rev. Lett. **90**, 146801 (2003).

[27] B. A. Bernevig, J. Orenstein, and S.-C. Zhang, Exact SU(2) Symmetry and Persistent Spin Helix in a Spin-Orbit Coupled System, Phys. Rev. Lett. **97**, 236601 (2006).

[28] J. D. Koralek, C. P. Weber, J. Orenstein, B. A. Bernevig, S.-C. Zhang, S. Mack, and D. D. Awschalom, Emergence of the persistent spin helix in semiconductor quantum wells, Nature (London) **458**, 610 (2009).

[29] V. K. Kalevich and V. Korenev, Effect of electric field on the optical orientation of 2D electrons, JETP Lett. **52**, 230 (1990).

[30] Y. Kato, R. C. Myers, A. C. Gossard, and D. D. Awschalom, Coherent spin manipulation without magnetic fields in strained semiconductors, Nature (London) **427**, 50 (2004).

[31] L. Meier, G. Salis, I. Shorubalko, E. Gini, S. Schön, and K. Ensslin, Measurement of rashba and dresselhaus spin-orbit magnetic fields, Nat. Phys. **3**, 650 (2007).

[32] M. Studer, G. Salis, K. Ensslin, D. C. Driscoll, and A. C. Gossard, Gate-Controlled Spin-Orbit Interaction in a Parabolic GaAs/AlGaAs Quantum Well, Phys. Rev. Lett. **103**, 027201 (2009).

[33] P. S. Eldridge, J. Hübner, S. Oertel, R. T. Harley, M. Henini, and M. Oestreich, Spin-orbit fields in asymmetric (001)-oriented GaAs/Al_x Ga_{1-x} As quantum wells, Phys. Rev. B **83**, 041301(R) (2011).

[34] M. P. Walser, U. Siegenthaler, V. Lechner, D. Schuh, S. D. Ganichev, W. Wegscheider, and G. Salis, Dependence of the Dresselhaus spin-orbit interaction on the quantum well width, Phys. Rev. B **86**, 195309 (2012).

[35] J. Ishihara, Y. Ohno, and H. Ohno, Direct imaging of gate-controlled persistent spin helix state in a modulation-doped GaAs/AlGaAs quantum well, Appl. Phys. Express **7**, 013001 (2013).

[36] Y. Kunihashi, H. Sanada, H. Gotoh, K. Onomitsu, M. Kohda, J. Nitta, and T. Sogawa, Drift transport of helical spin coherence with tailored spin-orbit interactions, Nat. Commun. **7**, 10722 (2016).

[37] B. Das, D. C. Miller, S. Datta, R. Reifenberger, W. P. Hong, P. K. Bhattacharya, J. Singh, and M. Jaffe, Evidence for spin

splitting in $In_xGa_{1-x}As/In_{0.52}Ga_{0.48}As$ heterostructures for $B \rightarrow 0$, Phys. Rev. B **39**, 1411 (1989).

[38] S. Hikami, A. I. Larkin, and Y. Nagaoka, Spin-orbit interaction and magnetoresistance in the two dimensional random system, Prog. Theor. Phys. **63**, 707 (1980).

[39] B. L. Al'tshuler, A. G. Aronov, A. I. Larkin, and D. E. Khmel'nitskii, Anomalous magnetoresistance in semiconductors, J. Exp. Theor. Phys. **54**, 411 (1981).

[40] B. L. Altshuler, D. Khmel'nitzkii, A. I. Larkin, and P. A. Lee, Magnetoresistance and Hall effect in a disordered two-dimensional electron gas, Phys. Rev. B **22**, 5142 (1980).

[41] F. G. Pikus and G. E. Pikus, Conduction-band spin splitting and negative magnetoresistance in A_3B_5 heterostructures, Phys. Rev. B **51**, 16928 (1995).

[42] M. P. Walser, C. Reichl, W. Wegscheider, and G. Salis, Direct mapping of the formation of a persistent spin helix, Nat. Phys. **8**, 757 (2012).

[43] J. J. Krich and B. I. Halperin, Cubic Dresselhaus Spin-Orbit Coupling in 2D Electron Quantum Dots, Phys. Rev. Lett. **98**, 226802 (2007).

[44] D. J. English, J. Hübner, P. S. Eldridge, D. Taylor, M. Henini, R. T. Harley, and M. Oestreich, Effect of symmetry reduction on the spin dynamics of (001)-oriented GaAs quantum wells, Phys. Rev. B **87**, 075304 (2013).

[45] P. Altmann, F. G. G. Hernandez, G. J. Ferreira, M. Kohda, C. Reichl, W. Wegscheider, and G. Salis, Current-Controlled Spin Precession of Quasistationary Electrons in a Cubic Spin-Orbit Field, Phys. Rev. Lett. **116**, 196802 (2016).

[46] S. Maekawa and H. Fukuyama, Magnetoresistance in two-dimensional disordered systems: Effects of zeeman splitting and spin-orbit scattering, J. Phys. Soc. Jpn. **50**, 2516 (1981).

[47] M. D'yakonov, V. Marushchal, V. Perel', and A. Titkov, The effect of strain on the spin relaxation of conduction electrons in Ill-V semiconductors, JETP Lett. **63**, 655 (1986).

[48] S. Iordanskii, Y. Lyanda-Geller, and G. Pikus, Weak Localization in Quantum Wells with Spin-Orbit Interaction, JETP Lett. **60**, 199 (1994).

[49] W. Knap, C. Skierbiszewski, A. Zduniak, E. Litwin-Staszewska, D. Bertho, F. Kobbi, J. L. Robert, G. E. Pikus, F. G. Pikus, S. V. Iordanskii, V. Mosser, K. Zekentes, and Y. B. Lyanda-Geller, Weak antilocalization and spin precession in quantum wells, Phys. Rev. B **53**, 3912 (1996).

[50] A. Punnoose, Magnetoconductivity in the presence of bychkov-rashba spin-orbit interaction, Appl. Phys. Lett. **88**, 252113 (2006).

[51] D. C. Marinescu, Cubic Dresselhaus interaction parameter from quantum corrections to the conductivity in the presence of an in-plane magnetic field, Phys. Rev. B **96**, 115109 (2017).

[52] A. Kawabata, On the field dependence of magnetoresistance in two-dimensional systems, J. Phys. Soc. Jpn. **53**, 3540 (1984).

[53] A. Zduniak, M. I. Dyakonov, and W. Knap, Universal behavior of magnetoconductance due to weak localization in two dimensions, Phys. Rev. B **56**, 1996 (1997).

[54] J. B. Miller, D. M. Zumbühl, C. M. Marcus, Y. B. Lyanda-Geller, D. Goldhaber-Gordon, K. Campman, and A. C. Gossard, Gate-Controlled Spin-Orbit Quantum Interference Effects in Lateral Transport, Phys. Rev. Lett. **90**, 076807 (2003).

[55] L. E. Golub, Weak antilocalization in high-mobility two-dimensional systems, Phys. Rev. B **71**, 235310 (2005).

[56] M. M. Glazov and L. E. Golub, Nondiffusive weak localization in two-dimensional systems with spin-orbit splitting of the spectrum, Semiconductors **40**, 1209 (2006).

[57] M. M. Glazov and L. E. Golub, Spin-orbit interaction and weak localization in heterostructures, Semicond. Sci. Technol. **24**, 064007 (2009).

[58] A. Sawada and T. Koga, Universal modeling of weak antilocalization corrections in quasi-two-dimensional electron systems using predetermined return orbitals, Phys. Rev. E **95**, 023309 (2017).

[59] S. Kettemann, Dimensional Control of Antilocalization and Spin Relaxation in Quantum Wires, Phys. Rev. Lett. **98**, 176808 (2007).

[60] M. Kammermeier, P. Wenk, and J. Schliemann, Control of Spin Helix Symmetry in Semiconductor Quantum Wells by Crystal Orientation, Phys. Rev. Lett. **117**, 236801 (2016).

[61] E. Bernardes, J. Schliemann, M. Lee, J. C. Egues, and D. Loss, Spin-Orbit Interaction in Symmetric Wells with Two Subbands, Phys. Rev. Lett. **99**, 076603 (2007).

[62] J. Fu, P. H. Penteado, M. O. Hachiya, D. Loss, and J. C. Egues, Persistent Skyrmion Lattice of Noninteracting Electrons with Spin-Orbit Coupling, Phys. Rev. Lett. **117**, 226401 (2016).

[63] D. C. Marinescu, P. J. Weigele, D. M. Zumbühl, and J. C. Egues, Closed-Form Weak Localization Magnetoconductivity in Quantum Wells with Arbitrary Rashba and Dresselhaus Spin-Orbit Interactions, Phys. Rev. Lett. **122**, 156601 (2019).

[64] J. Rammer, *Quantum Transport Theory*, Frontiers in Physics Vol. 99 (Perseus Books, Reading, Massachusetts, 1998).

[65] S. Das Sarma and F. Stern, Single-particle relaxation time versus scattering time in an impure electron gas, Phys. Rev. B **32**, 8442 (1985).

[66] P. T. Coleridge, Small-angle scattering in two-dimensional electron gases, Phys. Rev. B **44**, 3793 (1991).

[67] D. M. Zumbühl, J. B. Miller, C. M. Marcus, K. Campman, and A. C. Gossard, Spin-Orbit Coupling, Antilocalization, and Parallel Magnetic Fields in Quantum Dots, Phys. Rev. Lett. **89**, 276803 (2002).

[68] D. M. Zumbühl, J. B. Miller, C. M. Marcus, V. I. Fal'ko, T. Jungwirth, and J. S. Harris, Jr., Orbital effects of in-plane magnetic fields probed by mesoscopic conductance fluctuations, Phys. Rev. B **69**, 121305(R) (2004).

[69] D. M. Zumbühl, J. B. Miller, C. M. Marcus, D. Goldhaber-Gordon, J. S. Harris, K. Campman, and A. C. Gossard, Conductance fluctuations and partially broken spin symmetries in quantum dots, Phys. Rev. B **72**, 081305(R) (2005).

[70] See Supplemental Material at http://link.aps.org/supplemental/10.1103/PhysRevB.101.035414 for the derivation of the quantum corrections to conductivity, a full account of the data sets, and details on the fit procedure, including Ref. [81].

[71] B. L. Al'tshuler and A. Aronov, Electron-electron interactions in disorder conductors, *Modern Problems in Condensed Matter Sciences*, Vol. 10 (Elsevier, Gatchina, Leningrad, 1985), pp. 1–153.

[72] L. Casparis, M. Meschke, D. Maradan, A. C. Clark, C. P. Scheller, K. K. Schwarzwälder, J. P. Pekola, and D. M. Zumbühl, Metallic Coulomb blockade thermometry down to 10 mK and below, Rev. Sci. Instrum. **83**, 083903 (2012).

[73] D. Maradan, L. Casparis, T. M. Liu, D. E. F. Biesinger, C. P. Scheller, D. M. Zumbühl, J. Zimmerman, and A. C. Gossard,

GaAs quantum dot thermometry using direct transport and charge sensing, J. Low Temp. Phys. **175**, 784 (2014).

[74] A. G. Huibers, M. Switkes, C. M. Marcus, K. Campman, and A. C. Gossard, Dephasing in Open Quantum Dots, Phys. Rev. Lett. **81**, 200 (1998).

[75] A. G. Huibers, J. A. Folk, S. R. Patel, C. M. Marcus, C. I. Duruöz, and J. S. Harris, Low-Temperature Saturation of the Dephasing Time and Effects of Microwave Radiation on Open Quantum Dots, Phys. Rev. Lett. **83**, 5090 (1999).

[76] S. Faniel, T. Matsuura, S. Mineshige, Y. Sekine, and T. Koga, Determination of spin-orbit coefficients in semiconductor quantum wells, Phys. Rev. B **83**, 115309 (2011).

[77] A. N. Chantis, M. van Schilfgaarde, and T. Kotani, *Ab Initio* Prediction of Conduction Band Spin Splitting in Zinc Blende Semiconductors, Phys. Rev. Lett. **96**, 086405 (2006).

[78] M. Gmitra and J. Fabian, First-principles studies of orbital and spin-orbit properties of GaAs, GaSb, InAs, and InSb zinc-blende and wurtzite semiconductors, Phys. Rev. B **94**, 165202 (2016).

[79] R. S. Calsaverini, E. Bernardes, J. C. Egues, and D. Loss, Intersubband-induced spin-orbit interaction in quantum wells, Phys. Rev. B **78**, 155313 (2008).

[80] K. D. Maranowski, J. P. Ibbetson, K. L. Campman, and A. C. Gossard, Interface between low-temperature grown GaAs and undoped GaAs as a conduction barrier for back gates, Appl. Phys. Lett. **66**, 3459 (1995).

[81] L. Gor'kov, A. Larkin, and D. Khmel'nitskii, Particle conductivity in a two-dimensional random potential, JETP Lett. **30**, 228 (1979).